



# SCIENTIFIC REPORTS



OPEN

## Facile Solution Synthesis of Tungsten Trioxide Doped with Nanocrystalline Molybdenum Trioxide for Electrochromic Devices

Amirhossein Hasani<sup>1</sup>, Quyet Van Le<sup>1</sup>, Thang Phan Nguyen<sup>1</sup>, Kyoung Soon Choi<sup>2</sup>, Woonbae Sohn<sup>3</sup>, Jang-Kyo Kim<sup>4</sup>, Ho Won Jang<sup>1</sup> <sup>3</sup> & Soo Young Kim<sup>1</sup> <sup>1</sup>

A facile, highly efficient approach to obtain molybdenum trioxide (MoO<sub>3</sub>)-doped tungsten trioxide (WO<sub>3</sub>) is reported. An annealing process was used to transform ammonium tetrathiotungstate [(NH<sub>4</sub>)<sub>2</sub>WS<sub>4</sub>] to WO<sub>3</sub> in the presence of oxygen. Ammonium tetrathiomolybdate [(NH<sub>4</sub>)<sub>2</sub>MoS<sub>4</sub>] was used as a dopant to improve the film for use in an electrochromic (EC) cell. (NH<sub>4</sub>)<sub>2</sub>MoS<sub>4</sub> at different concentrations (10, 20, 30, and 40 mM) was added to the (NH<sub>4</sub>)<sub>2</sub>WS<sub>4</sub> precursor by sonication and the samples were annealed at 500 °C in air. Raman, X-ray diffraction, and X-ray photoelectron spectroscopy measurements confirmed that the (NH<sub>4</sub>)<sub>2</sub>WS<sub>4</sub> precursor decomposed to WO<sub>3</sub> and the (NH<sub>4</sub>)<sub>2</sub>MoS<sub>4</sub>–(NH<sub>4</sub>)<sub>2</sub>WS<sub>4</sub> precursor was transformed to MoO<sub>3</sub>-doped WO<sub>3</sub> after annealing at 500 °C. It is shown that the MoO<sub>3</sub>-doped WO<sub>3</sub> film is more uniform and porous than pure WO<sub>3</sub>, confirming the doping quality and the privileges of the proposed method. The optimal MoO<sub>3</sub>-doped WO<sub>3</sub> used as an EC layer exhibited a high coloration efficiency of 128.1 cm<sup>2</sup>/C, which is larger than that of pure WO<sub>3</sub> (74.5 cm<sup>2</sup>/C). Therefore, MoO<sub>3</sub>-doped WO<sub>3</sub> synthesized by the reported method is a promising candidate for high-efficiency and low-cost smart windows.

Electrochromic (EC) materials have attracted much attention owing to their potential applications in smart windows, antiglare mirrors, data storage devices, displays, sunroofs, and sunglasses. Various materials can be used as an EC layer, including inorganic metal oxides and organic conducting polymers<sup>1–8</sup>.

Conducting polymers provide benefits such as multiple colors, a fast switching time, and flexibility, but their disadvantages, including relatively nonuniform films, low material stability, and a limited range of colors severely limit their practical applications<sup>9,10</sup>. On the other hand, tungsten trioxide (WO<sub>3</sub>) is a well-known metal oxide owing to its excellent EC performance. WO<sub>3</sub> with different structures has been prepared by techniques such as hydrothermal process, chemical vapor deposition, thermal evaporation, and sputtering<sup>11–15</sup>. However, these approaches have drawbacks that restrict the commercial application of WO<sub>3</sub> EC films, including complicated preparation, high energy consumption, expensive equipment, or the use of toxic and dangerous reagents<sup>16</sup>.

Molybdenum oxide is one of the important semiconducting metal oxides and can be used in various applications, including photovoltaic cells, organic light-emitting diodes, gas sensors, hydrogen evolution systems, transistors, and EC devices<sup>17–22</sup>. However, the coloration efficiency of pure molybdenum oxide used in EC devices is not high. For example, Patil *et al.* found that MoO<sub>3</sub> used as an EC layer had a coloration efficiency of 34 cm<sup>2</sup>/C<sup>23</sup>. A combination of tungsten and molybdenum oxide has been used in EC devices recently. For instance, Mahdavi *et al.* investigated the effect of molybdenum in a WO<sub>3</sub> thin film prepared by RF magnetron sputtering and obtained

<sup>1</sup>School of Chemical Engineering and Materials Science, Integrative research center for two-dimensional functional materials, Institute of Interdisciplinary Convergence Research, Chung-Ang University, 84 Heukseok-ro, Dongjak-gu, Seoul, 06974, Republic of Korea. <sup>2</sup>Advanced Nano-Surface Research Group, Korea Basic Science Institute (KBSI), 169-148, Gwahak-ro, Yuseong-gu, Daejeon, 34133, Republic of Korea. <sup>3</sup>Department of Materials Science and Engineering, Research Institute of Advanced Materials, Seoul National University, Seoul, 08826, Republic of Korea. <sup>4</sup>Department of Mechanical Engineering, The Hong Kong University of Science and Technology, Clear Water Bay, Kowloon, Hong Kong, P.R. China. Amirhossein Hasani and Quyet Van Le contributed equally to this work. Correspondence and requests for materials should be addressed to H.W.J. (email: [hwjang@snu.ac.kr](mailto:hwjang@snu.ac.kr)) or S.Y.K. (email: [sooyoungkim@cau.ac.kr](mailto:sooyoungkim@cau.ac.kr))

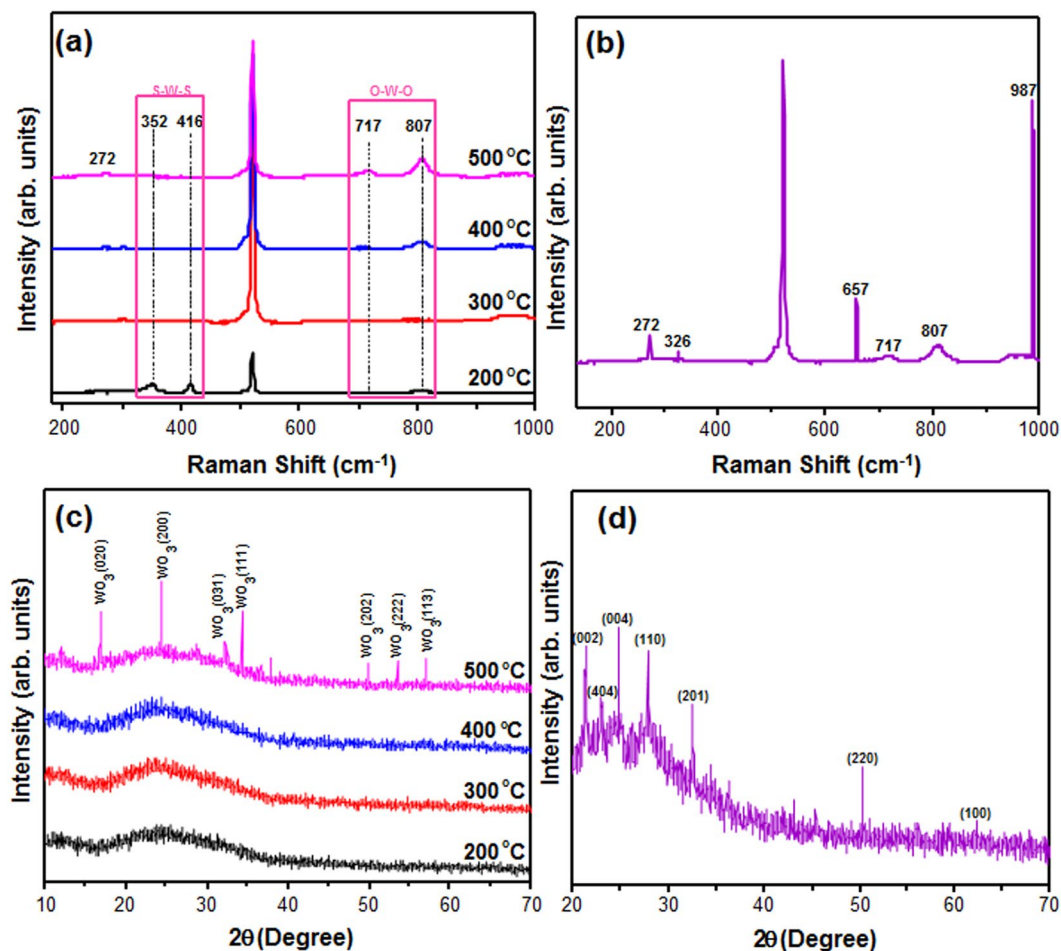


**Figure 1.** (a) Raman spectra of  $(\text{NH}_4)_2\text{WS}_4$  films annealed at different temperatures, (b) Raman spectra of  $(\text{NH}_4)_2\text{WS}_4/(\text{NH}_4)_2\text{MoS}_4$  (30 mM) film annealed at 500 °C, (c) XRD pattern of  $(\text{NH}_4)_2\text{WS}_4$  film annealed at different temperatures, (d) XRD pattern of  $(\text{NH}_4)_2\text{WS}_4/(\text{NH}_4)_2\text{MoS}_4$  (30 mM) film annealed at 500 °C.

a coloration efficiency of  $42.5 \text{ cm}^2/\text{C}^{24}$ . Kharade *et al.* synthesized  $\text{MoO}_3$  mixed with  $\text{WO}_3$  using a hybrid physico-chemical method and achieved a high coloration efficiency of  $121.56 \text{ cm}^2/\text{C}^{25}$ . However, the complicated synthesis method with high cost is a drawback. Consequently, it is urgently necessary to develop immediate, effective, and facile methods to synthesize tungsten oxide films with enhanced EC performance.

In this study, we report a facile, low-cost method of producing EC thin films based on  $\text{WO}_3$  for smart window applications. In our previous work, we investigated the  $(\text{NH}_4)_2\text{WS}_4$  precursor annealed at 350 °C as a hole transport layer in an organic solar cell<sup>26</sup>. In this work, we investigate the use of different annealing temperatures to obtain  $\text{WO}_3$ , and then we add the  $(\text{NH}_4)_2\text{MoS}_4$  precursor as a dopant to the  $(\text{NH}_4)_2\text{WS}_4$  precursor at different concentrations (10, 20, 30, and 40 mM) to obtain optimal EC films. A spin-coating method with an annealing process was applied to obtain EC films with excellent features such as high EC energy efficiency, high coloration efficiency, low cost, excellent chemical stability, fast switching speed, and good adhesion to the substrate.

## Results and Discussion

The Raman spectra of the  $(\text{NH}_4)_2\text{WS}_4$  films annealed at different temperatures are shown in Fig. 1(a). The Raman peak of the S–W–S stretching mode is weakened for the amorphous phase as the temperature is increased, whereas the peaks corresponding to  $\text{WO}_3$  phases (O–W–O bending and stretching) are strengthened<sup>27</sup>. Therefore, the  $\text{WO}_3$  phases are completely decomposed after annealing at 500 °C, indicating a monoclinic crystal system. Figure 1(b) shows the Raman spectra of the  $\text{MoO}_3$ -doped  $\text{WO}_3$  film. The peak at  $675 \text{ cm}^{-1}$  is ascribed to the coordinated oxygen in Mo crystal structure and stretching mode, which confirms that  $(\text{NH}_4)_2\text{MoS}_4$  was transformed to a  $\text{MoO}_3$  crystal, as indicated by the edge-shared oxygen<sup>28</sup>. Moreover, the Raman peaks at  $272 \text{ cm}^{-1}$  is assigned to O=Mo=O wagging modes<sup>28</sup>. Fig. 1(c) shows the XRD patterns of  $(\text{NH}_4)_2\text{WS}_4$  thin films annealed at different temperatures. The pristine  $\text{WS}_4$  shows broad  $\text{WS}_2$  peaks ( $2\theta = 15\text{--}35^\circ$ ) related to weak crystallinity at annealing temperatures below 400 °C. The broad peak intensity decreases after annealing at 500 °C, and the peaks corresponding to  $\text{WO}_3$  structure are observed as well. These peaks are quite similar to those reported for monoclinic  $\text{WO}_3$ <sup>29</sup>. Fig. 1(d) confirms the nanocrystallinity of the  $\text{MoO}_3$ -doped  $\text{WO}_3$  films. The molybdenum is incorporated into the film, producing a new phase with orthorhombic crystal structure which is similar to the

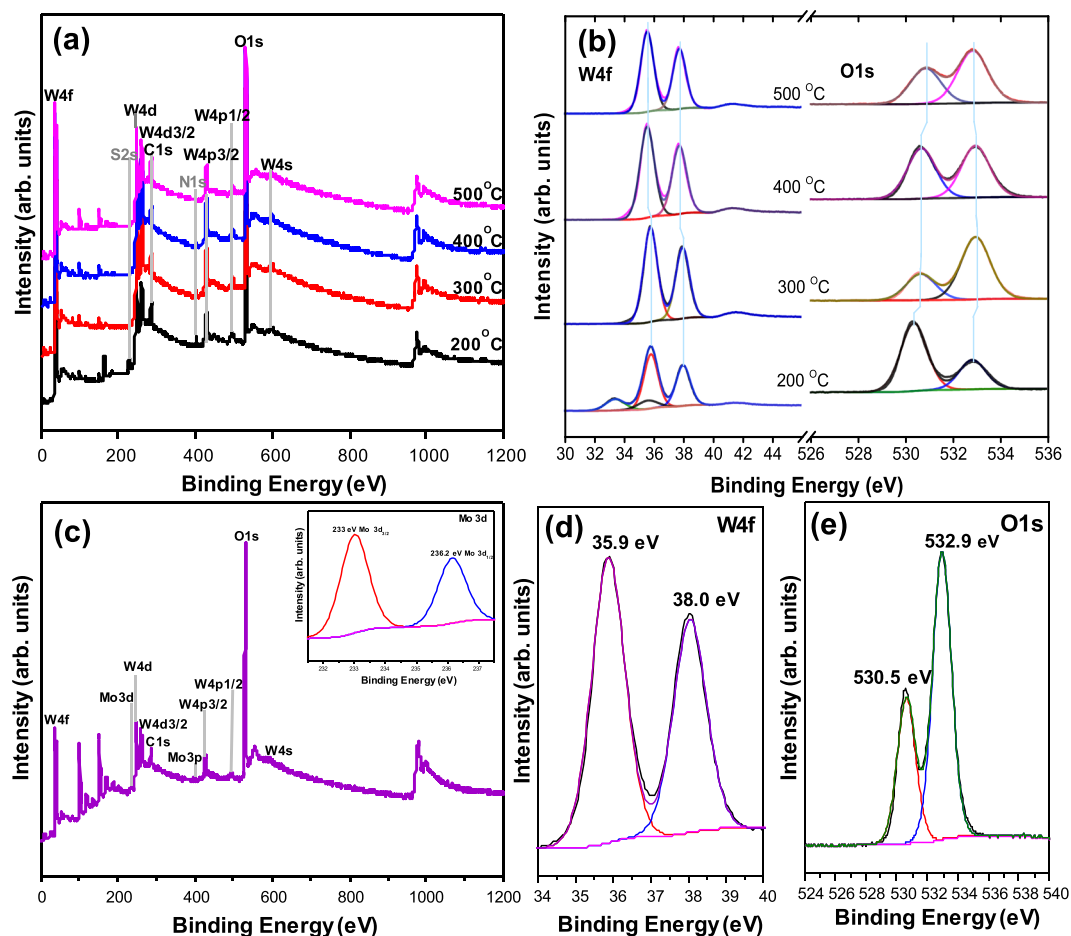


**Figure 2.** (a) XPS survey spectra of  $(\text{NH}_4)_2\text{WS}_4$  films annealed at different temperatures, (b) high-resolution W 4f and O 1s spectra of  $(\text{NH}_4)_2\text{WS}_4$  films annealed at different temperatures, (c) XPS survey spectra of  $(\text{NH}_4)_2\text{WS}_4/(\text{NH}_4)_2\text{MoS}_4$  (30 mM) film annealed at 500 °C with high-resolution Mo 3d spectrum (inset), (d) W 4f and (e) O 1s spectra of  $(\text{NH}_4)_2\text{WS}_4/(\text{NH}_4)_2\text{MoS}_4$  (30 mM) film annealed at 500 °C.

previously reported structures<sup>24,30</sup>. Moreover, the XRD results of the  $\text{MoO}_3$ -doped  $\text{WO}_3$  did not show the peaks related to metallic Mo or  $\text{MoO}_3$ , suggesting the well-diffusion of molybdenum atoms into  $\text{WO}_3$  crystal structure and substitution of Mo in W sites<sup>24</sup>.

The XPS spectra of  $(\text{NH}_4)_2\text{WS}_4$  films annealed at different temperatures are shown in Fig. 2(a). As the temperature increases to 500 °C, the S 2s and N 1s peaks related to the  $(\text{NH}_4)_2\text{WS}_4$  precursor disappear, suggesting the complete decomposition of the  $(\text{NH}_4)_2\text{WS}_4$  precursor into  $\text{WO}_3$ .  $\text{WO}_3$  appears owing to the presence of  $\text{O}_2$  in the air<sup>26</sup>. High-resolution views of the W 4f and O 1s peaks are shown in Fig. 2(b). The peak appears at 33.5 eV for the  $(\text{NH}_4)_2\text{WS}_4$  film annealed at 200 °C, and the peaks at 35.4, 36.3, and 38 eV are ascribed to  $\text{W}^{4+}$ ,  $\text{W}^{5+}$ , and  $\text{W}^{6+}$ <sup>26</sup>. The peak of  $\text{W}^{5+}$  is related to oxygen vacancy<sup>31</sup>. As the annealing temperature increases, the peak located at 33.5 eV vanishes, confirming the transformation of  $\text{WS}_2$  to  $\text{WO}_3$ . The observed shifts of the peaks in the O 1s and W 4f spectra toward lower binding energy can be attributed to the emission of photoelectrons from the higher to lower oxidation states of W<sup>32</sup>. For the XPS data in the O 1s region, the peak density related to the oxide phase near 531 eV increases as the annealing temperature increases beyond 300 °C (Fig. 2(b))<sup>33</sup>. The XPS survey scan of the  $\text{MoO}_3$ -doped  $\text{WO}_3$  film (Fig. 2(c)) shows additional peaks that are related to Mo 3d and Mo 3p. The XPS peak positions of Mo 3d<sub>3/2</sub> and Mo 3d<sub>5/2</sub> are 233 and 236.2 eV, respectively (inset of Fig. 2(c)), which are attributed to pair of orbital spinning of  $\text{MoO}_3$ <sup>34</sup>. The two observed peaks of W 4f<sub>7/2</sub> and W 4f<sub>5/2</sub> appear at 35.9 and 38 eV, respectively (Fig. 2(d)). Figure 2(e) shows the high-resolution XPS O 1s spectrum, in which the oxygen O 1s peaks are observed at 530.5 and 539.2 eV. The spectra indicate the presence of W, Mo, and O in the as-prepared  $\text{MoO}_3$ -doped  $\text{WO}_3$  EC film with oxidation states of +6, +6, and -2, respectively<sup>25</sup>. All of XPS results and observed peaks are confirmed by previously reported works<sup>25–35</sup>.

The atomic ratios of  $(\text{NH}_4)_2\text{WS}_4$  films annealed at different temperatures are shown in Fig. 3(a). Those of sulfur (S 2s) and nitrogen (N 1s) approach zero as the annealing temperature is increased to 400 °C. The pie chart in Fig. 3(b) indicates that the oxygen content of the  $\text{MoO}_3$ -doped  $\text{WO}_3$  is higher than that of other atoms owing to the annealing process and the presence of oxygen in both the  $\text{MoO}_3$  and  $\text{WO}_3$  structures. It is calculated that the level of doping was 0.76% (30 mM  $(\text{NH}_4)_2\text{MoS}_4$  into  $(\text{NH}_4)_2\text{WS}_4$  precursor). These results not only support the formation of an oxide surface layer on the sulfide  $(\text{NH}_4)_2\text{WS}_4$  backbone, but also represent the functionalization of  $\text{MoO}_3$  on the  $\text{WO}_3$  structure. As shown in the inset of Fig. 3(c), the work function of the pure  $\text{WO}_3$  thin film

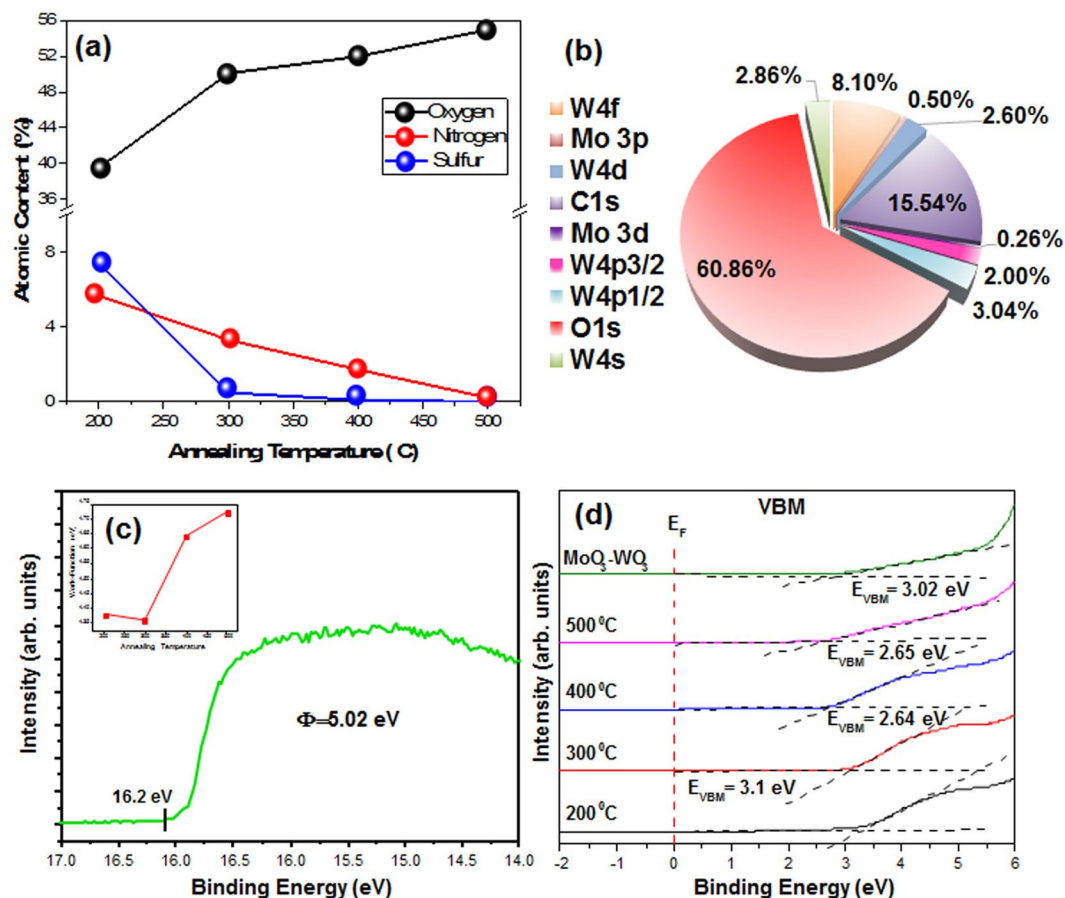


**Figure 3.** (a) Atomic ratios of  $(\text{NH}_4)_2\text{WS}_4$  films annealed at different temperatures, (b) atomic content of  $(\text{NH}_4)_2\text{WS}_4/(\text{NH}_4)_2\text{MoS}_4$  (30 mM) film annealed at 500 °C, (c) UPS spectra of  $(\text{NH}_4)_2\text{WS}_4/(\text{NH}_4)_2\text{MoS}_4$  (30 mM) film annealed at 500 °C and (inset) work function of  $(\text{NH}_4)_2\text{WS}_4$  films annealed at different temperatures, (d) ultraviolet photoelectron spectra of  $(\text{NH}_4)_2\text{WS}_4$  films annealed at different temperatures and  $(\text{NH}_4)_2\text{WS}_4/(\text{NH}_4)_2\text{MoS}_4$  (30 mM) film annealed at 500 °C.

increases as the annealing temperature increased to 500 °C. The work function of  $\text{WO}_3$  at 500 °C is 4.71 eV (inset of Fig. 3(c)). The increase of work function is attributed to the formation of  $\text{WO}_3$ <sup>26</sup>. In addition, the green curve shown in Fig. 3(c) indicates that the work function of  $\text{MoO}_3$ -doped  $\text{WO}_3$  at 500 °C is 5.02 eV, which is higher than that pure  $\text{WO}_3$ . These data suggest better performance of electrochromic in  $\text{MoO}_3$ -doped  $\text{WO}_3$  device by facilitating charge transfer. Figure 3(d) shows the valance band maxima (VBMs) of the  $\text{WO}_3$  and  $\text{MoO}_3$ -doped  $\text{WO}_3$ , which decrease with increasing annealing temperature. However,  $\text{MoO}_3$  doping method increases the VBM owing to changes in the O 1s states and promoting the transition of intervalance within metal ions<sup>34,36</sup>. These data suggest the enhanced transition of electron in  $\text{MoO}_3$ -doped  $\text{WO}_3$  film, resulting in increased coloration efficiency.

Figure 4 shows FESEM and HRTEM images of the  $\text{WO}_3$  and  $\text{MoO}_3$ -doped  $\text{WO}_3$ . Both samples have porous and compact surfaces. The observed cracks are attributed to the annealing process (Fig. 4(a) and (b)). Moreover, the  $\text{MoO}_3$ -doped  $\text{WO}_3$  exhibits a more uniform than pure  $\text{WO}_3$  (Fig. 4(c)). In addition, porosity measurement was carried out by using MATLAB software whose method was previously reported<sup>37</sup>. In order to measure the porosity, the FESEM images of  $\text{WO}_3$  and  $\text{MoO}_3$ -doped  $\text{WO}_3$  were converted to binary image (see Figure S1) and then the percentage of porosity was calculated by following formula:

$$P = \left(1 - \frac{n}{N}\right) \times 100 \quad (1)$$

where P is the porosity percent, n is the number of white pixels, and N is the total number of white and black pixels. The percentage of porosities were obtained 58.2 and 75.6% in  $\text{WO}_3$  and  $\text{MoO}_3$ -doped  $\text{WO}_3$  film, respectively. The lattice fringes in the HRTEM images demonstrate that the  $\text{WO}_3$  films are crystallized, confirming the XRD results. In addition, the estimated lattice spacings of 0.302 and 0.364 nm are assigned to the monoclinic d-spacing of the (020) plane of  $\text{WO}_3$  and the orthorhombic (002) plane of  $\text{MoO}_3$  (Fig. 4(d) and (e)). Figure 4(f) shows the elemental distributions of W, O, and Mo for the  $\text{MoO}_3$ -doped  $\text{WO}_3$  thin film.  $\text{MoO}_3$  atoms not only grew on the  $\text{WO}_3$  surface, but are also diffused into the film. These data indicate that the method has great potential for efficient doping.

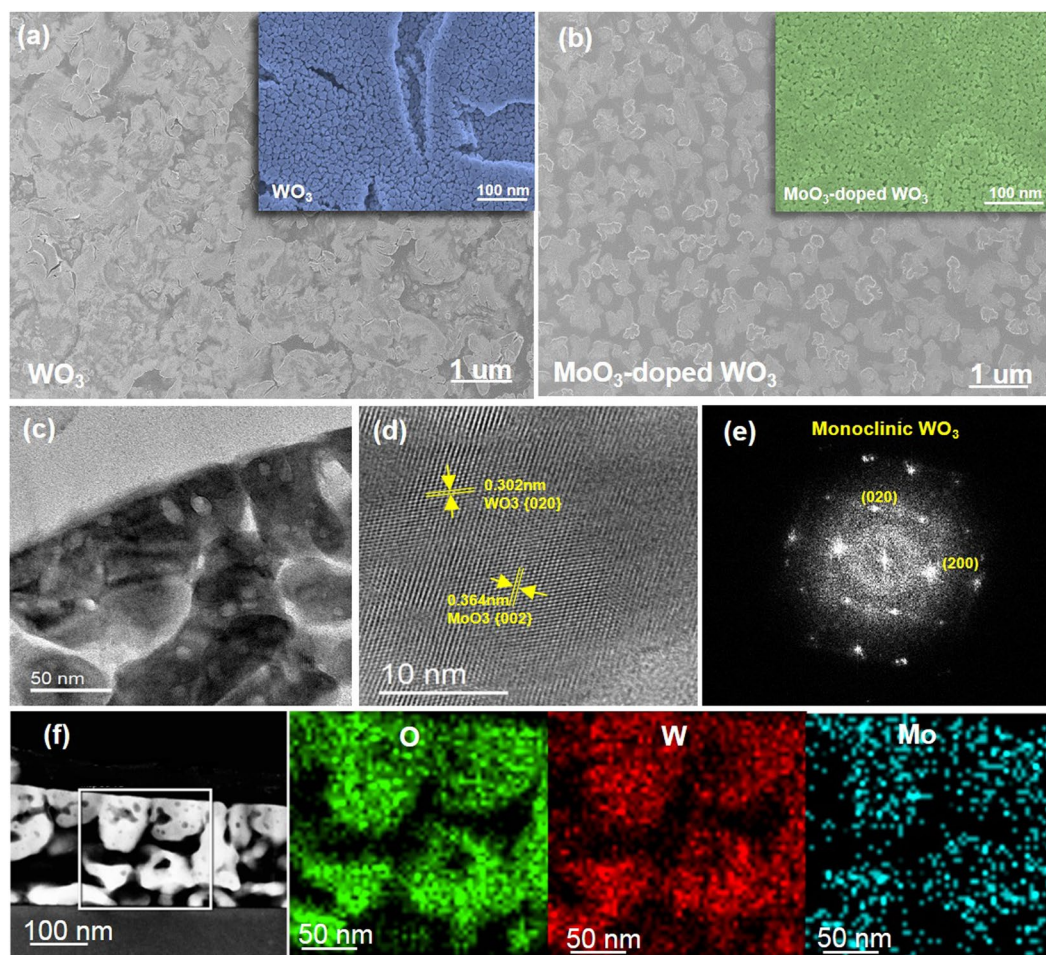


**Figure 4.** FESEM images of (a)  $(\text{NH}_4)_2\text{WS}_4$  film and (b)  $(\text{NH}_4)_2\text{WS}_4/(\text{NH}_4)_2\text{MoS}_4$  (30 mM) film annealed at 500 °C, (c) TEM image of  $\text{MoO}_3$ -doped  $\text{WO}_3$ , (d) HRTEM image of  $\text{MoO}_3$ -doped  $\text{WO}_3$ , (e) electron diffraction and (f) STEM images and the corresponding STEM-EDX elemental maps of  $\text{MoO}_3$ -doped  $\text{WO}_3$ .

According to the AFM images (Fig. 5), the measured roughness of the  $\text{WO}_3$  and  $\text{MoO}_3$ -doped  $\text{WO}_3$  is 6.5 and 2.4 nm, respectively. Therefore, the uniformity of film is increased without aggregation caused by doping. The AFM images confirm that the porosity of the film is greater after doping. The higher porosity is expected to improve the EC performance by enhancing the diffusion constant of the intercalating ions through the pore interface<sup>38</sup>. In addition, higher roughness and porosity of film can improve the distribution of electrical field during redox process resulting in enhanced electron transfer and ion-insertion, leading to high EC performance<sup>24,34,39,40</sup>.

Figure 6(a) shows the configuration of the EC cell. The transmittance spectra (wavelength 400–900 nm) of  $\text{WO}_3$  and  $\text{MoO}_3$ -doped  $\text{WO}_3$  in the colored and bleached states were measured (Fig. 6(b)). The color was changed to dark blue when a DC voltage of  $-2.5$  V was applied across the ITO. After the voltage was changed to  $+2.5$  V, the EC cell returned to the transparent state. The mechanism is thought to be the oxidation and reduction process.  $\text{Li}^+$  ions are inserted into the EC film, leading to reduction of  $\text{W}^{6+}$  to  $\text{W}^{5+}$  and the increase in the cathodic current change the color of the film. The change from the colored state to the transparent state is ascribed to oxidation ( $\text{W}^{5+}$  to  $\text{W}^{6+}$ ) due to the changing in redox state of the tungsten ions and the number of electrons (charge) inserted into EC film<sup>24</sup>. In the doped EC film, Mo is involved in the reduction/oxidation process ( $\text{Mo}^{6+}$  to  $\text{Mo}^{5+}$  and  $\text{Mo}^{5+}$  to  $\text{Mo}^{6+}$ ), which causes to the enhanced transition of intervalency and electron transition within ions<sup>34</sup>. Optical modulation is one of the most important parameters in EC devices and can be defined as  $\Delta T = T_b - T_c$ , where  $T_b$  and  $T_c$  are the transmittance in the bleached and colored states, respectively, at a particular wavelength<sup>41</sup>. The difference in transmission ( $\Delta T$  at 675 nm) between the bleached and colored states in  $\text{WO}_3$  and  $\text{MoO}_3$ -doped  $\text{WO}_3$  was enhanced from  $\Delta T_1 = 35\%$  to  $\Delta T_2 = 49\%$ . This improvement is attributed to a change in the crystal structure of  $\text{WO}_3$  caused by substitution of Mo at W sites and charge transfer between the  $\text{Mo}^{5+}$  and  $\text{W}^{6+}$  sites<sup>24,42</sup>. Fig. 6(c) shows the stability of the  $\text{WO}_3$  and  $\text{MoO}_3$ -doped  $\text{WO}_3$  in the colored state for several weeks after the voltage is removed.  $\text{MoO}_3$ -doped  $\text{WO}_3$  exhibited better memory behaviour in air, in which it relatively retained the colored state very well even after 4 weeks. On the other hand, some parts of the pure  $\text{WO}_3$  EC film became transparent as time passed. Therefore, the memory behaviour of  $\text{MoO}_3$ -doped  $\text{WO}_3$  is better than that of pure  $\text{WO}_3$  because of the increase in the diffusion coefficient ( $D$ ) of  $\text{Li}^+$  ions in  $\text{MoO}_3$ -doped  $\text{WO}_3$  during the intercalation process<sup>24</sup>. Diffusion coefficient during intercalation process can be calculated by Randles–Sevcik equation<sup>24,43</sup>:

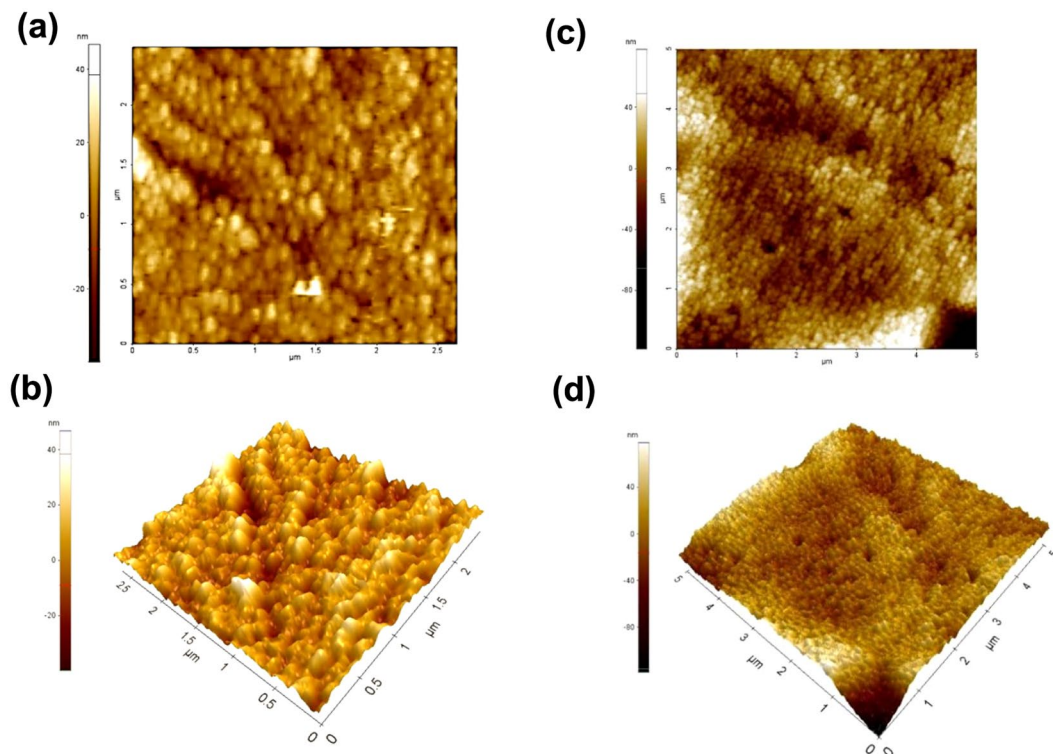


**Figure 5.** (a) 2D and (b) 3D AFM images of  $(\text{NH}_4)_2\text{WS}_4$  film annealed at  $500^\circ\text{C}$ , (c) 2D and (d) 3D AFM images of  $(\text{NH}_4)_2\text{WS}_4/(\text{NH}_4)_2\text{MoS}_4$  (30 mM) film annealed at  $500^\circ\text{C}$ .

$$D^{1/2} = i_p / [(2.72 \times 10^5) n^{3/2} A C_0 \pi r^2 \nu^{1/2}] \quad (2)$$

where  $i_p$  is the anodic peak current density,  $n$  is the number of electrons transferred during redox process,  $C_0$  is the concentration of active ions in the electrolyte,  $\nu$  is the scan rate, and  $A$  is the area of the EC film<sup>24</sup>. The diffusion coefficient was obtained  $1.23 \times 10^{-11}$  and  $9.42 \times 10^{-11}$  for the  $\text{WO}_3$  and  $\text{MoO}_3$ -doped  $\text{WO}_3$  EC film, respectively. Figure 6(d) and (e) shows the current-voltage (CV) curves of pure  $\text{WO}_3$  and  $\text{MoO}_3$ -doped  $\text{WO}_3$  thin films, which were measured in a 1 M aqueous solution at a scan rate of 50 mV/s. In the cathodic process, the current of pure  $\text{WO}_3$  is higher than that of the  $\text{MoO}_3$ -doped  $\text{WO}_3$  thin film. The  $\text{MoO}_3$ -doped  $\text{WO}_3$  has a higher conductivity than pure  $\text{WO}_3$  because more defect states are created owing to integration of the two metal oxides, decreasing the energy required to extract the intercalated  $\text{Li}^+$  ions after  $\text{MoO}_3$  doping<sup>24,25</sup>. In addition, the cycling stability of both thin films after 300 cycle steps revealed that the current in the  $\text{MoO}_3$ -doped  $\text{WO}_3$  did not change and remained constant compared to that of the pure  $\text{WO}_3$  EC film. Moreover, the CV curves not only indicate a well-crystallized  $\text{WO}_3$  structure in both films, but also confirm the XRD and TEM results.

The coloration efficiency (CE), which is an important parameter for EC devices, was calculated as follows<sup>23,24,30</sup>:

$$\text{CE} = \frac{\Delta\text{OD}}{Q} \quad (3)$$

$$\Delta\text{OD} = \log \left[ \frac{T_b}{T_c} \right] \quad (4)$$

where  $\Delta\text{OD}$  is the change in optical density,  $Q$  is the charge density,  $T_b$  is the transmittance of the film in the bleached state, and  $T_c$  is the transmittance of the film in the colored state<sup>23,24,41</sup>. The color efficiency of various EC layers and various  $\text{MoO}_3$  concentrations ( $\lambda = 675 \text{ nm}$ ) is presented in Fig. 6(f). The CE values of the  $\text{MoO}_3$ -doped  $\text{WO}_3$  are higher than that of pure  $\text{WO}_3$  ( $74.5 \text{ cm}^2/\text{C}$ ). To determine the optimal concentration of  $\text{MoO}_3$  in  $\text{WO}_3$ , the CE was measured for different  $\text{MoO}_3$  concentrations (10, 20, 30, and 40 mM) in  $\text{WO}_3$ . As shown in Fig. 6(f), a much higher CE ( $128.1 \text{ cm}^2/\text{C}$ ) was obtained for the  $\text{MoO}_3$ -doped  $\text{WO}_3$  with a  $\text{MoO}_3$  concentration of 30 mM. This result indicates that the optimal amount of molybdenum has a crucial role in obtaining high efficiency. Furthermore, the response times of the colored and bleached states for  $\text{MoO}_3$ -doped  $\text{WO}_3$  are found to be 3.6 and 4.5 s, respectively, whereas the response times of the colored and bleached states for pure as-prepared  $\text{WO}_3$  are 8 and 9.5 s, respectively. Enhanced EC properties is caused by improvement in extra electron intervalance transfer  $\text{W}^{6+}$  and  $\text{Mo}^{6+}$  active sites. In addition, molybdenum after intercalation of  $\text{Li}^+$  ions are more near to the sensitivity of human's vision. The disorder could be increased by random distribution of molybdenum, resulting

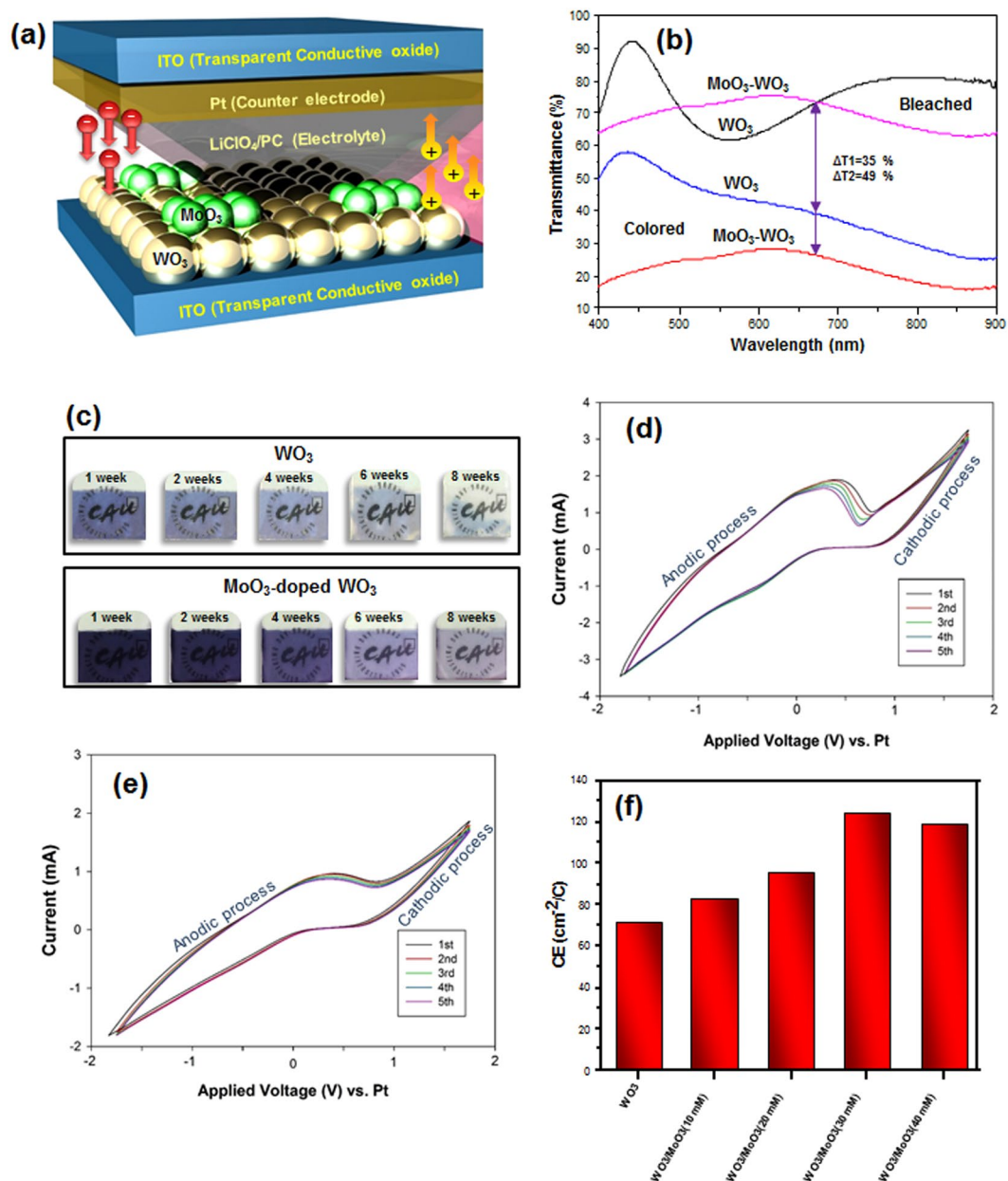


**Figure 6.** (a) Structure of as-prepared EC cell, (b) transmission spectra of WO<sub>3</sub> and MoO<sub>3</sub>-doped WO<sub>3</sub>, (c) memory behavior of WO<sub>3</sub> and MoO<sub>3</sub>-doped WO<sub>3</sub> films during 8 weeks, CV curves of (d) WO<sub>3</sub> and (e) MoO<sub>3</sub>-doped WO<sub>3</sub> EC films and (f) coloration efficiency of the different EC films.

in the betterment EC properties<sup>25</sup>. Therefore, the performance was improved by MoO<sub>3</sub> doping. Table 1 compares our results with the reported values through various materials and methods.

## Conclusions

WO<sub>3</sub> doped with MoO<sub>3</sub> was prepared by a facile and low-cost method involving solution and annealing processes. The results indicated that the (NH<sub>4</sub>)<sub>2</sub>MoS<sub>4</sub>/(NH<sub>4</sub>)<sub>2</sub>WS<sub>4</sub> precursor decomposed to MoO<sub>3</sub>-doped WO<sub>3</sub> when the film was annealed at 500 °C in air. The N 1s and S 2s emission in the XPS spectrum of the (NH<sub>4</sub>)<sub>2</sub>WS<sub>4</sub> precursor annealed at 500 °C, as well as weakening of the S–W–S bond, increased O–W–O bond peaks in the Raman spectra, and the appearance of peaks in the XRD spectra, suggested full decomposition to monoclinic crystalline WO<sub>3</sub>. In addition, (NH<sub>4</sub>)<sub>2</sub>MoS<sub>4</sub> was added to the (NH<sub>4</sub>)<sub>2</sub>WS<sub>4</sub> precursor at various concentrations as a dopant, and the resulting films were then annealed at 500 °C to transform them to MoO<sub>3</sub>-doped WO<sub>3</sub>. The XRD and Raman spectroscopy results confirmed the decomposition to nanocrystalline MoO<sub>3</sub>-doped WO<sub>3</sub>. Moreover, the morphology of the as-prepared films was observed using FESEM and AFM, which showed that the MoO<sub>3</sub>-doped WO<sub>3</sub> was more uniform and porous than pure WO<sub>3</sub>, suggesting high EC performance. Furthermore, the high doping capability with good distribution of MoO<sub>3</sub> into WO<sub>3</sub> was confirmed by HRTEM images. As a result, enhanced

Material	Method	Switching time ( $t_c/t_b$ )	$\Delta T$ (%)	Coloration efficiency ( $\text{cm}^2/\text{C}$ )	Ref.
Mo-doped $\text{WO}_3$	RF magnetron sputtering	—	44.3	42.5	24
$\text{MoO}_3/\text{WO}_3$	Hybrid physicochemical synthesis	4.1 s/3.4 s	~50	121.56	25
Nanoparticulate $\text{WO}_3$	Electrodeposition	3.7 s/5.2 s	88.51	137	35
$\text{NiO}/\text{WO}_3$	DC magnetron sputtering	10 s/20 s	55	87	40
Ti-doped $\text{WO}_3$	Sol-gel spin-coating	—	47.5	—	44
PANI/ $\text{WO}_3$	Electropolymerization	9.9 s/13.6 s	37.4	98.4	45
$\text{WO}_x$ nanorods	Low-temperature ozone exposure	11.8 s/20.1 s	57	33.3	46
WONWS-RGO	Solothermal	1.5 s/1.2 s	—	116.7	47
$\text{MoO}_3$ -doped $\text{WO}_3$	Solution and annealing process	3.6 s/4.5 s	49	128.1	Our work

**Table 1.** Comparison of our work with previously published papers.

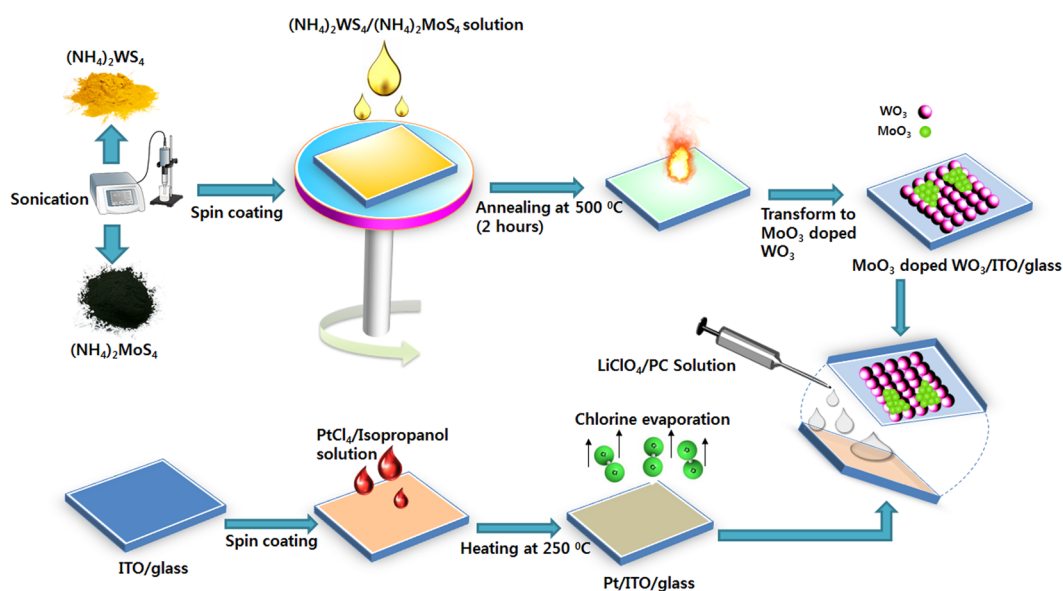


**Figure 7.** Synthesis of EC materials and fabrication of EC cell.

EC performance was obtained when the  $\text{MoO}_3$ -doped (30 mM)  $\text{WO}_3$  was used as an EC layer. The coloration efficiency was high ( $\text{CE} = 128.1 \text{ cm}^2/\text{C}$ ), and the response time was rapid ( $t_c = 3 \text{ s}$ ,  $t_b = 4.5 \text{ s}$ ). These values are much higher than those of pure  $\text{WO}_3$  ( $\text{CE} = 74.5 \text{ cm}^2/\text{C}$ ,  $t_c = 8 \text{ s}$ ,  $t_b = 9.5 \text{ s}$ ). In conclusion, the  $\text{MoO}_3$ -doped  $\text{WO}_3$  prepared by the annealing–solution process is a remarkable candidate for use in high-efficiency, low-cost smart windows that can be efficiently commercialized.

## Method

**Preparation of thin film of  $\text{MoO}_3$ -doped  $\text{WO}_3$ .** Figure 7 illustrates the synthesis of the  $\text{WO}_3$  and  $\text{MoO}_3$ -doped  $\text{WO}_3$  thin films and fabrication of the EC cell. Indium tin oxide (ITO) substrates were ultrasonically cleaned sequentially with DI water, isopropanol, and acetone, and then dried; they were then treated by ultraviolet ozone for 20 min and maintained there until the start of the spin-coating process. After drying,  $\text{PtCl}_4$  dispersed in isopropanol was coated on one piece of the ITO conductive glass by spin-coating, and the ITO was dried on a hotplate at  $250^\circ\text{C}$  to evaporate the solvent and chlorine; this sample was used as a counter electrode. Next,  $(\text{NH}_4)_2\text{WS}_4$  (200 mg) was dissolved in 1 ml of *N,N*-dimethylformamide, resulting in the formation of a yellowish tungsten sol. Then, a homogenous thin film was prepared by spin-coating the as-prepared solution onto the ITO substrate at 4000 rpm for 60 s. After drying in air, the coated substrates were annealed in a furnace at different temperatures (200, 300, 400, and  $500^\circ\text{C}$ ) for 2 h. A transparent, colorless  $\text{WO}_3$  thin film was obtained at  $500^\circ\text{C}$ . To form the  $\text{MoO}_3$ -doped  $\text{WO}_3$  thin films,  $(\text{NH}_4)_2\text{MoS}_4$  was added to the  $(\text{NH}_4)_2\text{WS}_4$  solution separately (at different concentrations, 10, 20, 30, and 40 mM, to determine the optimal amount of doping) to form a homogenous solution. Then, this procedure was repeated to synthesize  $\text{MoO}_3$ -doped  $\text{WO}_3$  thin films at  $500^\circ\text{C}$ .

**Fabrication of the EC cell.** The EC device structure for the  $\text{MoO}_3$ -doped  $\text{WO}_3$  thin films was glass/ITO/ $\text{MoO}_3$ -doped  $\text{WO}_3$ /LiClO<sub>4</sub> + propylene carbonate (PC)/Pt/ITO/glass. The ITO substrate coated with the  $\text{MoO}_3$ -doped  $\text{WO}_3$  thin film acts as a working electrode, and the Pt/ITO-coated conducting glass substrate acts as a counter electrode; the electrodes are assembled to fabricate a sandwich-type EC device. The liquid electrolyte, 1 M lithium perchlorate (LiClO<sub>4</sub>)/PC, was injected into the device through a small hole, which was then sealed with Resibond epoxy glue.



**Characterizations.** X-ray photoelectron spectroscopy (XPS) was performed using an ESCA-3000 (VG Scientific Ltd., England) instrument analyzer under a vacuum better than  $1 \times 10^{-5}$  mbar using Mg K $\alpha$  radiation (1250 eV) and a constant pass energy of 50 eV. The composition of the thin film samples was determined by X-ray diffraction (XRD) analysis (Bruker AXS Model D8 Advance X-ray diffractometer) with a Cu K $\alpha$  target having a wavelength 0.1542 nm. Raman spectra (LabRAM HR, Horiba Jobin Yvon, Japan) were obtained at an exciting wavelength of 514 nm. Field-emission scanning electron microscopy (FESEM, Zeiss 300 VP) images were taken at an acceleration voltage of 50 kV. Transmission electron microscopy (TEM) was performed with a JEOL-2100F (Japan) instrument. Contact-mode atomic force microscopy (AFM, XE-100/PSIA) was used to determine the roughness and porosity of the thin films. Cyclic voltammetry (CV) and electrochemical measurements were performed in a quartz electrochemical cell connected to a potentiostat (Ivium 5612, Netherlands). WO<sub>3</sub> or MoO<sub>3</sub>-doped WO<sub>3</sub> was used as the working electrode, and a Ag/AgCl electrode and platinum (Pt) wire were applied as the reference and counter electrodes, respectively. The transmittance spectra were measured by a UV-vis spectrophotometer (V-670). The coloration/bleaching switching characteristics of the EC films were recorded as the changes in the transmittance at a wavelength of 675 nm under alternating application of a potential of  $\pm 2.5$  V for 60 s for each state. For the XPS, high-resolution TEM (HRTEM), FESEM, XRD, Raman, and AFM measurements of the MoO<sub>3</sub>-doped WO<sub>3</sub>, samples fabricated using 30 mM of (NH<sub>4</sub>)<sub>2</sub>MoS<sub>4</sub> in the (NH<sub>4</sub>)<sub>2</sub>WS<sub>4</sub> precursor were used.

## References

1. Runnerstrom, E. L. *et al.* Nanostructured electrochromic smart windows: traditional materials and NIR-selective plasmonic nanocrystals. *Chem. Commun.* **50**, 10555–10572, <https://doi.org/10.1039/c4cc03109a> (2014).
2. Tajima, K., Hotta, H., Yamada, Y., Okada, M. & Yoshimura, K. Electrochromic switchable mirror glass with controllable reflectance. *Appl. Phys. Lett.* **100**, doi:Artn 09190610.1063/1.3691256 (2012).
3. Wang, K. *et al.* Integrated energy storage and electrochromic function in one flexible device: an energy storage smart window. *Energ. Environ. Sci.* **5**, 8384–8389, <https://doi.org/10.1039/c2ee21643d> (2012).
4. Cheng, C. P. *et al.* Performance improvement of electrochromic display devices employing micro-size precipitates of tungsten oxide. *Appl. Phys. A* **116**, 1553–1559, <https://doi.org/10.1007/s00339-014-8371-x> (2014).
5. Ma, C. *et al.* Smart sunglasses based on electrochromic polymers. *Polym. Eng. Sci.* **48**, 2224–2228 (2008).
6. Lampert, C. M. Chromogenic smart materials. *Mater. Today* **7**, 28–35, [https://doi.org/10.1016/S1369-7021\(04\)00123-3](https://doi.org/10.1016/S1369-7021(04)00123-3) (2004).
7. Xiong, S. *et al.* Organic/inorganic electrochromic nanocomposites with various interfacial interactions: A review. *Mater. Sci. Eng. B* **221**, 41–53, <https://doi.org/10.1016/j.mseb.2017.03.017> (2017).
8. Sassi, M. *et al.* Organic electrochromic polymers: state-of-the-art neutral tint multichromophoric polymers for high-contrast see-through electrochromic devices. *Adv. Funct. Mater.* **26**, 5239–5239, <https://doi.org/10.1002/adfm.201601819> (2016).
9. Yuksel, R. *et al.* Silver nanowire/conducting polymer nanocomposite electrochromic supercapacitor electrodes. *J. Electrochem. Soc.* **164**, A721–A727, <https://doi.org/10.1149/2.0791704jes> (2017).
10. Liang, Y., Strohecker, D., Lynch, V. M., Holliday, B. J. & Jones, R. A. A thiophene-containing conductive metallopolymer using an Fe (II) Bis (terpyridine) core for electrochromic materials. *ACS Appl. Mater. Interfaces* **8**, doi:<https://doi.org/10.1021/acsami.6b11657> (2016).
11. Su, X. *et al.* Synthesis of uniform WO<sub>3</sub> square nanoplates via an organic acid-assisted hydrothermal process. *Mater. Lett.* **64**, 1232–1234, <https://doi.org/10.1016/j.matlet.2010.02.063> (2010).
12. Marsen, B. *et al.* Progress in sputtered tungsten trioxide for photoelectrode applications. *Int. J. Hydrogen Energy* **32**, 3110–3115, <https://doi.org/10.1016/j.ijhydene.2006.01.022> (2007).
13. Gogova, D. *et al.* Structural and optical properties of CVD thin tungsten oxide films. *Physical Status Solidi A* **176**, 969–984, doi:10.1002/(SICI)1521-396X(199912)176:2<969::AID-PSSA969>3.0.CO;2-9 (1999).
14. Ponzoni, A. *et al.* Nanostructured WO<sub>3</sub> deposited by modified thermal evaporation for gas-sensing applications. *Thin Solid Films* **490**, 81–85, <https://doi.org/10.1016/j.tsf.2005.04.031> (2005).
15. Leftheriotis, G. *et al.* Structural and electrochemical properties of opaque sol-gel deposited WO<sub>3</sub> layers. *Appl. Surf. Sci.* **218**, 276–281, [https://doi.org/10.1016/S0169-4332\(03\)00616-0](https://doi.org/10.1016/S0169-4332(03)00616-0) (2003).
16. Xie, Z. *et al.* Fast fabrication of a WO<sub>3</sub>·2H<sub>2</sub>O thin film with improved electrochromic properties. *J. Mater. Chem.* **22**, 19904–19910, <https://doi.org/10.1039/C2JM33622G> (2012).
17. Kwon, K. C. *et al.* Wafer-scale transferable molybdenum disulfide thin-film catalysts for photoelectrochemical hydrogen production. *Energ. Environ. Sci.* **9**, 2240–2248, <https://doi.org/10.1039/C6EE00144K> (2016).
18. Kim, Y. H. *et al.* Ultrasensitive reversible oxygen sensing by using liquid-exfoliated MoS<sub>2</sub> nanoparticles. *J. Mater. Chem. A* **4**, 6070–6076, <https://doi.org/10.1039/C6TA01277A> (2016).
19. Nguyen, T. P. *et al.* MoS<sub>2</sub> nanosheets exfoliated by sonication and their application in organic photovoltaic cells. *Sci Adv. Mater.* **7**, 700–705, <https://doi.org/10.1166/sam.2015.1891> (2015).
20. Van, L. Q. *et al.* The use of UV/ozone-treated MoS<sub>2</sub> nanosheets for extended air stability in organic photovoltaic cells. *Phys. Chem. Chem. Phys.* **16**, 13123–13128, <https://doi.org/10.1039/c4cp01598c> (2014).
21. Kim, S. *et al.* High-mobility and low-power thin-film transistors based on multilayer MoS<sub>2</sub> crystals. *Nat. Commun.* **3**, 1011, <https://doi.org/10.1038/ncomms2018> (2012).
22. Jeon, P. J. *et al.* Low power consumption complementary inverters with n-MoS<sub>2</sub> and p-WSe<sub>2</sub> dichalcogenide nanosheets on glass for logic and light-emitting diode circuits. *ACS Appl. Mater. Inter.* **7**, 22333–22340, <https://doi.org/10.1021/acsami.5b06027> (2015).
23. Patil, R. S. *et al.* Electrosynthesis of electrochromic molybdenum oxide thin films with rod-like features. *Int. J. Electrochem. Sci.* **3**, 259–265 (2008).
24. Madhavi, V., Kumar, P. J., Kondaiah, P., Hussain, O. M. & Uthanna, S. Effect of molybdenum doping on the electrochromic properties of tungsten oxide thin films by RF magnetron sputtering. *Ionics* **20**, 1737–1745, <https://doi.org/10.1007/s11581-014-1073-8> (2014).
25. Kharade, R. R. *et al.* Hybrid physicochemical synthesis and electrochromic performance of WO<sub>3</sub>/MoO<sub>3</sub> thin films. *Electroanal.* **26**, 2388–2397, <https://doi.org/10.1002/elan.201400239> (2014).
26. Le, Q. V. *et al.* (NH<sub>4</sub>)<sub>2</sub>WS<sub>4</sub> precursor as a hole-injection layer in organic optoelectronic devices. *Chem Eng J* **284**, 285–293, <https://doi.org/10.1016/j.cej.2015.08.142> (2016).
27. Xu, L. J., Yin, M. L. & Liu, S. Z. Agx@WO<sub>3</sub> core-shell nanostructure for LSP enhanced chemical sensors. *Sci Rep-Uk* **4**, doi:ARTN 674510.1038/srep06745 (2014).
28. Sharma, R. K. & Reddy, G. B. Synthesis and characterization of alpha-MoO<sub>3</sub> microspheres packed with nanoflakes. *J. Phys. D: Appl. Phys.* **47**, <https://doi.org/10.1088/0022-3727/47/6/065305> (2014).
29. Balzer, R. *et al.* Synthesis and structure-activity relationship of a WO<sub>3</sub> catalyst for the total oxidation of BTX. *J. Brazil. Chem. Soc.* **25**, 2026–2031, <https://doi.org/10.5935/0103-5053.20140187> (2014).
30. Zhang, H., Li, Y., Duan, G., Liu, G. & Cai, W. Tungsten oxide nanostructures based on laser ablation in water and a hydrothermal route. *Cryst. Eng. Comm.* **16**, 2491–2498, <https://doi.org/10.1039/C3CE42320D> (2014).

31. Li, Y., Tang, Z., Zhang, J. & Zhang, Z. Defect engineering of air-treated WO<sub>3</sub> and Its enhanced visible-light-driven photocatalytic and electrochemical performance. *J. Phys. Chem. C* **120**, 9750–9763, <https://doi.org/10.1021/acs.jpcc.6b00457> (2016).
32. Vuong, N. M., Kim, D. & Kim, H. Porous Au-embedded WO<sub>3</sub> nanowire structure for efficient detection of CH<sub>4</sub> and H<sub>2</sub>S. *Sci Rep-Uk* **5**, <https://doi.org/10.1038/srep11040> (2015).
33. Ryu, W.-H. *et al.* Heterogeneous WSx/WO<sub>3</sub> thorn-bush nanofiber electrodes for sodium-ion batteries. *ACS Nano* **10**, 3257–3266, <https://doi.org/10.1021/acsnano.5b06538> (2016).
34. Dong, W. *et al.* Bifunctional MoO<sub>3</sub>-WO<sub>3</sub>/Ag/MoO<sub>3</sub>-WO<sub>3</sub> films for efficient ITO-free electrochromic devices. *ACS Appl. Mater. Inter.* **8**, 33842–33847, <https://doi.org/10.1021/acsmi.6b12346> (2016).
35. Dalavi, D. S. *et al.* Efficient electrochromic performance of nanoparticulate WO<sub>3</sub> thin films. *J. Mater. Chem. C* **1**, 3722–3728, <https://doi.org/10.1039/C3TC30378K> (2013).
36. White, R. T., Thibau, E. S. & Lu, Z.-H. Interface structure of MoO<sub>3</sub> on organic semiconductors. *Sci Rep-Uk* **6**, <https://doi.org/10.1038/srep21109> (2016).
37. Entekhabi, E., Nazarpak, M. H., Moztarzadeh, F. & Sadeghi, A. Design and manufacture of neural tissue engineering scaffolds using hyaluronic acid and polycaprolactone nanofibers with controlled porosity. *Mater. Sci. Eng. C* **69**, 380–387, <https://doi.org/10.1016/j.msec.2016.06.078> (2016).
38. Balaji, S. *et al.* Porous orthorhombic tungsten oxide thin films: synthesis, characterization, and application in electrochromic and photochromic devices. *J. Mater. Chem.* **21**, 3940–3948, <https://doi.org/10.1039/C0JM03773G> (2011).
39. Luo, W., Fu, X. K. & Ma, L. H. The research on the high quality TiO<sub>2</sub>, MoO<sub>3</sub>-doped WO<sub>3</sub> electrochromic film. *Chinese. Chem. Lett.* **18**, 883–886, <https://doi.org/10.1016/j.ccl.2007.05.003> (2007).
40. Zhang, J., Tu, J., Xia, X., Qiao, Y. & Lu, Y. An all-solid-state electrochromic device based on NiO/WO<sub>3</sub> complementary structure and solid hybrid polyelectrolyte. *Sol. Energ. Mat. Sol. C* **93**, 1840–1845, <https://doi.org/10.1016/j.solmat.2009.06.025> (2009).
41. Granqvist, C. G. *Handbook of inorganic electrochromic materials.* (Elsevier, 1995).
42. Yao, J., Loo, B., Hashimoto, K. & Fujishima, A. Photochromic characteristics of mixed WO<sub>3</sub>-MoO<sub>3</sub> thin films in alcohol vapors. *Berichte der Bunsengesellschaft für physikalische Chemie* **95**, 554–556, <https://doi.org/10.1002/bbpc.19910950502> (1991).
43. Nicholson, R. S. Theory and application of cyclic voltammetry for measurement of electrode reaction kinetics. *Anal. Chem.* **37**, 1351–1355, <https://doi.org/10.1021/ac60230a016> (1965).
44. Paipitak, K. *et al.* Characterization of sol-gel derived Ti-doped tungsten oxide electrochromic thin films. *Energy. procedia.* **9**, 446–451, <https://doi.org/10.1016/j.egypro.2011.09.050> (2011).
45. Wei, H. *et al.* Electropolymerized polyaniline stabilized tungsten oxide nanocomposite films: electrochromic behavior and electrochemical energy storage. *J. Phys. Chem. C* **116**, 25052–25064, <https://doi.org/10.1021/jp3090777> (2012).
46. Lin, F. *et al.* Low-temperature ozone exposure technique to modulate the stoichiometry of WO<sub>x</sub> nanorods and optimize the electrochromic performance. *Nanotechnology* **23**, 255601, <https://doi.org/10.1088/0957-4484/23/25/255601> (2012).
47. Chang, X., Sun, S., Dong, L., Hu, X. & Yin, Y. Tungsten oxide nanowires grown on graphene oxide sheets as high-performance electrochromic material. *Electrochim. Acta* **129**, 40–46, <https://doi.org/10.1016/j.electacta.2014.02.065> (2014).

## Acknowledgements

This research was supported in part by National Research Foundation of Korea (NRF) grants provided by the Korean government (MSIP) (Nos 2015K1A3A1A59073839, 2017H1D8A1030599, 2017K1A3A1A67014432) and in part by Korea Agency for Infrastructure Technology Advancement grant funded by Ministry of Land, Infrastructure and Transport (17IFIP-B133622-01).

## Author Contributions

A.H. and Q.V.L. contributed equally to this work. A.H. and Q.V.L. performed the synthesized materials and most of characterization. T.P.N., K.S.C., and W.S. performed device characterization. J.K.K. analyzed materials' characterization. H.W.J. and S.Y.K. supervised the experiments and contributed to manuscript preparation. H.W.J. and S.Y.K. initiated and directed the research. S.Y.K. conceived the idea and designed the experiments. All authors were involved in writing the manuscript.

## Additional Information

**Supplementary information** accompanies this paper at <https://doi.org/10.1038/s41598-017-13341-z>.

**Competing Interests:** The authors declare that they have no competing interests.

**Publisher's note:** Springer Nature remains neutral with regard to jurisdictional claims in published maps and institutional affiliations.



**Open Access** This article is licensed under a Creative Commons Attribution 4.0 International License, which permits use, sharing, adaptation, distribution and reproduction in any medium or format, as long as you give appropriate credit to the original author(s) and the source, provide a link to the Creative Commons license, and indicate if changes were made. The images or other third party material in this article are included in the article's Creative Commons license, unless indicated otherwise in a credit line to the material. If material is not included in the article's Creative Commons license and your intended use is not permitted by statutory regulation or exceeds the permitted use, you will need to obtain permission directly from the copyright holder. To view a copy of this license, visit <http://creativecommons.org/licenses/by/4.0/>.

© The Author(s) 2017